Structure
Article

The Structure and Assembly Mechanism of a Novel Three-Stranded Tubulin Filament that Centers Phage DNA

Elena A. Zehr,[1,3] James A. Kraemer,[1,3] Marcella L. Erb,[2] Joanna K.C. Coker,[2] Elizabeth A. Montabana,[1,4] Joe Pogliano,[2] and David A. Agard[1,*]
[1]Department of Biochemistry and Biophysics and the Howard Hughes Medical Institute, University of California, San Francisco, San Francisco, CA 94158, USA
[2]Division of Biological Sciences, University of California, San Diego, San Diego, CA 92093, USA
[3]These authors contributed equally to this work
[4]Present address: Department of Molecular and Cell Biology, University of California, Berkeley, Berkeley, CA 94720, USA
*Correspondence: agard@msg.ucsf.edu
http://dx.doi.org/10.1016/j.str.2014.02.006

SUMMARY

Tubulins are a universally conserved protein superfamily that carry out diverse biological roles by assembling filaments with very different architectures. The underlying basis of this structural diversity is poorly understood. Here, we determine a 7.1 Å cryo-electron microscopy reconstruction of the bacteriophage-encoded PhuZ filament and provide molecular-level insight into its cooperative assembly mechanism. The PhuZ family of tubulins is required to actively center the phage within infected host cells, facilitating efficient phage replication. Our reconstruction and derived model reveal the first example of a three-stranded tubulin filament. We show that the elongated C-terminal tail simultaneously stabilizes both longitudinal and lateral interactions, which in turn define filament architecture. Identified interaction surfaces are conserved within the PhuZ family, and their mutagenesis compromises polymerization in vitro and in vivo. Combining kinetic modeling of PhuZ filament assembly and structural data, we suggest a common filament structure and assembly mechanism for the PhuZ family of tubulins.

INTRODUCTION

Tubulins play diverse and critical roles in eukaryotic and prokaryotic cell biology. In eukaryotes, α/β-tubulin heterodimers typically assemble into 13-protofilament microtubules required for chromosome segregation and cellular trafficking. In contrast, monomers of FtsZ facilitate septation in bacteria and archaea via protofilaments, and perhaps sheet-like structures (Lu et al., 2000; Li et al., 2007; Aylett et al., 2011), and the plasmid segregation protein TubZ from *Bacillus thuringiensis* forms two- and four-stranded filaments (Aylett et al., 2010; Montabana and Agard, 2014). This remarkable diversity in polymer architecture is mirrored by a significant divergence in protein sequence, which leads to variations in the length of loops and the presence or absence of N/C-terminal extensions (Nogales et al., 1998a; Ni et al., 2010). However, the underlying physical basis for these differences in filament structure is only poorly understood.

Despite significant divergence in primary amino acid sequences, the core fold of the tubulin/FtsZ superfamily of proteins is highly conserved. The structure consists of the nucleotide-binding N-terminal domain and the activation domain, which facilitates guanosine triphosphate (GTP) hydrolysis via interaction of catalytic residues on the T7 loop, and H8 with the nucleotide-binding domain of the previous subunit in the filament. The two globular domains are separated by a long central helix, H7. Limited regions of strong sequence conservation are found in the loops required for GTP binding and hydrolysis, such as the G box, the T7 loop, and H8 (Nogales et al., 1998a). The divergent C-terminal tails of many tubulins are directly involved in binding associated factors and regulatory proteins (Aylett et al., 2011). Beyond these core structural elements, all tubulin homologs have a remarkably similar longitudinal (head-to-tail) mode of assembly (Nogales et al., 1998b; Löwe and Amos, 1999) that is dependent on GTP binding (Weisenberg, 1972; Bramhill and Thompson, 1994). Moreover, assembly juxtaposes the catalytic T7 loop of one subunit with the GTP exposed in the interface of the one below, thereby stimulating its hydrolysis.

Recently, a new set of tubulin-like proteins, encoded by bacteriophages, has been described (Oliva et al., 2012; Kraemer et al., 2012; Aylett et al., 2013). One of these proteins, PhuZ, from bacteriophage 201ϕ2-1 (hereafter referred to as $PhuZ_{201}$), was shown to form a highly dynamic, spindle-like cytoskeleton within infected *Pseudomonas chlororaphis* cells that functions to both cluster and center 201ϕ2-1 phage particles at the cell midpoint. Interfering with $PhuZ_{201}$ dynamics perturbs centering and compromises phage production (Kraemer et al., 2012). $PhuZ_{201}$ belongs to the PhuZ family of tubulin homologs (Kraemer et al., 2012), encoded by the genomes of very large bacteriophages from the "ϕKZ-like viruses" genus and the phage EL (Krylov et al., 2007; Lavigne et al., 2009). Virion particles of these giant *Pseudomonas* phages (211–317 kb in size) can have heads as large as 145 nm in diameter and 200 nm tails (Fokine et al., 2007). For such large viruses, diffusion within the host cell is likely quite restricted, perhaps explaining the reliance on a tubulin cytoskeletal element.

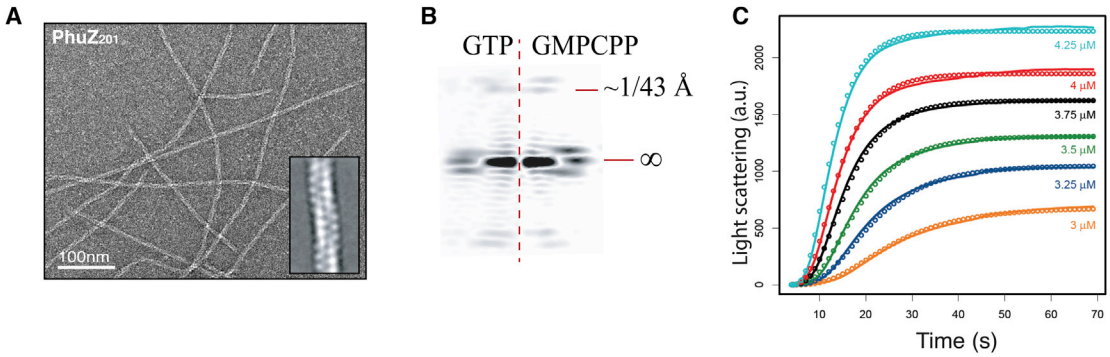

Figure 1. PhuZ$_{201}$ Assembles Three-Stranded Filaments and Forms a Hexameric Nucleus

(A) Section of a micrograph of negatively stained PhuZ$_{201}$ filaments polymerized in excess GMPCPP. Inset: reference-free 2D average of 500 segments of PhuZ$_{201}$ polymer.

(B) Fourier transforms of reference-free 2D averages of 500 segments of PhuZ$_{201}$ polymerized in 1 mM GTP (left) or 1 mM GMPCPP (right) show that the pitch of the filament is the same and is ~43 Å. (Left) GTP is hydrolyzed soon after assembly, resulting in PhuZ$_{201}$-GDP filaments.

(C) Determination of the nucleus size for PhuZ$_{201}$. PhuZ$_{201}$ was polymerized at varying concentrations in excess GTP. Solid lines are experimental data and circles are modeling results indicating a hexameric nucleus that grows by monomer and dimer addition.

The atomic structure of PhuZ$_{201}$ bound to guanosine diphosphate (GDP) showed that while PhuZ$_{201}$ has a conserved tubulin/FtsZ-like fold, it possesses several unique features, including an unusually long helix, H11, and an extended C terminus. PhuZ$_{201}$ also lacks H6, which contributes to longitudinal interactions in other tubulin homologs (Kraemer et al., 2012; Nogales et al., 1999), raising questions as to how PhuZ$_{201}$ forms filaments. Though the crystal lattice appeared to contain protofilaments, adjacent longitudinal subunits were separated far more than usual, forming a "relaxed" longitudinal interface, and the vast majority of intraprotofilament interactions were derived from the interactions between the C-terminal tail and the adjacent longitudinal subunit. Highly conserved acidic residues on the C-terminal tail of one subunit (the "acidic knuckle") make electrostatic contacts with a basic patch, formed by H3, H4, and H5, of its longitudinal neighbor. The importance of these C-terminal tail interactions for filament assembly was confirmed both in vitro and in vivo by mutagenesis (Kraemer et al., 2012). Together, these structural and functional results suggested a unique mechanism of filament assembly. Recently, atomic structures of a closely related PhuZ protein, PhuZ$_{KZ}$ (ϕKZ TubZ), encoded by the bacteriophage ϕKZ, were solved, revealing a high degree of structural similarity to PhuZ$_{201}$ and equivalent extensive longitudinal interactions mediated by the C-terminal tail, but with a more canonical tubulin/FtsZ "tense" longitudinal interface (Aylett et al., 2013).

In this work, we use cryo-electron microscopy (cryo-EM) to define the high-resolution three-dimensional (3D) architecture of a three-stranded tubulin filament and use a combination of solution polymerization measurements, kinetic modeling, and mutational analyses to confirm the relevance of this architecture in vitro and in vivo and to understand the PhuZ$_{201}$ assembly mechanism. On the basis of a derived pseudoatomic model and site-directed mutagenesis, conserved charged residues within the C terminus are identified that are essential for stabilizing three-stranded lateral interactions and filament assembly. These data allow us to propose a model for the structural origins of polymer metastability. Finally, by virtue of the high conservation of the residues that form filament contacts in PhuZ$_{201}$, we propose that the mechanism of PhuZ$_{201}$ filament assembly and its architecture are also conserved among the members of the PhuZ family.

RESULTS

PhuZ$_{201}$ Assembles Three-Stranded Filaments

To gain molecular insight into the mechanism of phage centering by PhuZ$_{201}$, we sought to determine the 3D filament structure by electron microscopy (EM). Although the filaments might have seemed to be two stranded at first, the unusual pattern of regular intensities along the filament axis seen in reference-free two-dimensional (2D) class averages of negatively stained PhuZ$_{201}$ filaments is more consistent with a three-stranded architecture (Figure 1A). These observations suggested a filament geometry distinct from that seen in the crystal (Kraemer et al., 2012). Fourier transforms of reference-free 2D averages of 500 segments of PhuZ$_{201}$ polymerized in either 1 mM GTP or the slowly hydrolysable GTP analog guanosine-5′-[(α,β)-methyleno]triphosphate (GMPCPP) looked indistinguishable, suggesting a similar filament architecture in the GDP or GTP state (Figure 1B). As a result, and to avoid potential structural heterogeneity resulting from variability in GTP hydrolysis, the reconstruction was performed on frozen-hydrated PhuZ$_{201}$ filaments assembled in the presence of 1 mM GMPCPP.

To look for complementary evidence of this unusual three-stranded organization and to gain insight into the assembly mechanism, PhuZ$_{201}$ growth kinetics were measured by right-angle light scattering at various concentrations in saturating (1 mM) GTP (Figure 1C). Polymerization experiments were carried out in BRB80 buffer (pH 7.2) to limit the formation of bundles, and the resultant critical concentration of 2.5 ± 0.1 μM was slightly lower than that previously reported for polymerization at pH 6.8 (Kraemer et al., 2012). No single-step model for progression to the nucleus, defined as the minimum number of monomers assembled for which polymerization is more favorable than depolymerization, fit the experimental data. Instead,

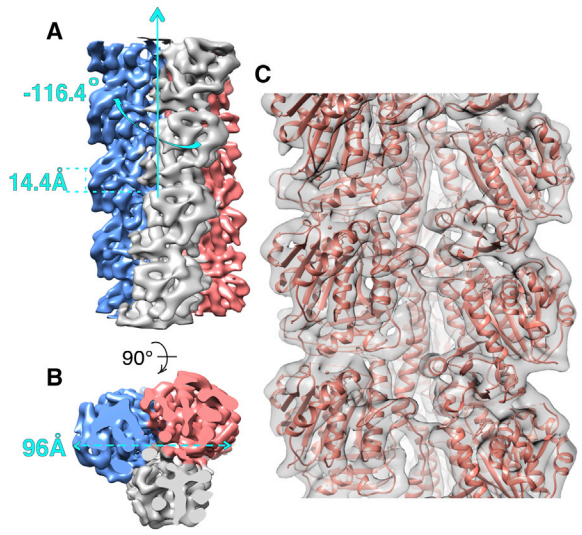

Figure 2. Cryo-EM Map and Pseudoatomic Model of PhuZ$_{201}$ Filament

(A and B) Cryo-EM map of PhuZ$_{201}$ filament with each protofilament presented in a different color. (A) Map has helical symmetry of −116.4° rotation and 14.4 Å rise per subunit. (B) End-on view of the filament shows that it is a trimer with 96 Å diameter.

(C) Pseudoatomic model of PhuZ$_{201}$ filament. In gray surface is the cryo-EM density fitted with the atomic models of PhuZ$_{201}$ in salmon.

See also Figure S1 and Movie S1.

a multistep formalism derived from that developed by Flyvbjerg et al. (1996), whereby multiple subunits can come together in multiple steps, was applied with modeling in Berkeley Madonna, a differential-equation-based modeling software package. The data were best described by a model wherein filaments form in two major kinetic steps: first bringing six monomers together, followed by further addition of a dimer. A nucleus size of six is consistent with a three-stranded filament, whereby forming two full layers would satisfy all intermonomer contacts required for growth.

Cryo-EM in conjunction with a single-particle helical analytic method (Frank et al., 1996; Egelman, 2000, 2007) was used to determine the 3D structure of the PhuZ$_{201}$-GMPCPP filament (Experimental Procedures). To better assess the resolution of the final map and to minimize overfitting, we used the "gold standard" procedure in which two separate reconstructions are independently developed from nonoverlapping halves of the data and then compared at each cycle to optimize estimation of the current resolution, and filtering for the next round of parameter refinement (Scheres and Chen, 2012). The final PhuZ$_{201}$ 3D map had a conservative resolution of 7.1 Å, based on the 0.5 Fourier shell correlation cutoff (Figure S1A available online), and had refined to the helical symmetry parameters of −116.4° rotation and 14.4 Å axial rise per subunit. The determined helical parameters were robust, as convergence to the same solution was achieved from different starting values of both helical parameters (Figure S1B and data not shown). Although the filament is a left-handed one-start helix, the azimuthal rotation of less than −120° per subunit results in an overall right-handed supertwist (Figure 2A). The hand of the supertwist was confirmed by tomography (data not shown). Moreover, computational experiments using different helical symmetries were done to demonstrate that all three strands were parallel (data not shown). The three-stranded architecture of the polymer is distinct from that of other cytomotive filaments characterized to date (Figure 2B).

PhuZ$_{201}$ Subunits Are Uniquely Oriented within the Filament

To interpret the cryo-EM map on a molecular level, a pseudoatomic model of the PhuZ$_{201}$ filament was built using the known atomic structure (Kraemer et al., 2012) (Figure 2C). At the obtained resolution, although individual β strands were not resolvable, all α helices, many loops, and the C-terminal tail (the most C-terminal 21 residues) could readily be fit, allowing unambiguous docking of the PhuZ$_{201}$ atomic model into the map. Fitting of the two globular domains and H7 separately into the map density resulted in a better fit to the map; the overall displacement was less than 1 Å, suggestive of slight conformational changes within the tubulin core. However, such simplistic fitting resulted in a worse fit for a number of loops, and we felt the resolution was insufficient to justify the significant rebuilding required. Consequently, we focus here on the compromise fit, treating the entire core as a single rigid body. In contrast, the C terminus (H11 and the C-terminal tail) required significant adjustments to fit into its corresponding cryo-EM density (Figure S1). Particularly, the acidic knuckle (the last 13 residues of the 21 residues of the C-terminal tail) (Kraemer et al., 2012) needed to be moved together with the upper subunit, which resulted in ∼6 Å displacement and 10.8° rotation of the knuckle toward the outer surface of the filament (Figure S1C). This preserved all of the acidic knuckle interactions observed in the crystal structure (Kraemer et al., 2012). An important consequence of this movement was to prevent clashes between the knuckle with H5 of the upper subunit and H9 of a subunit in the neighboring strand. To adapt to the movement, the rest of the tail structure needed to be repositioned toward the neighboring strand. Because the required motion was complex, a flexible fitting procedure was used (Supplemental Experimental Procedures), shifting residues F295 to I302 of the tail by on average 3.5 Å toward the adjacent strand to bring them into their map density (Figure S1D). Additionally, H11 was tilted by 6° toward the lumen to reposition it more upright within the three-stranded filament (Figure S1E). The overall correlation coefficient between the model and the map improved from a starting value of 0.610 to 0.640 after fitting.

The model of the PhuZ$_{201}$ filament (Figure 2C; Movie S1) revealed that the subunit orientation along the filament axis is unique, with the subunit rotated by ∼180° about the long axis of the filament when compared with the orientation of α/β-tubulin within microtubules and the orientation of the TubZ subunit within the four-stranded filament (Nogales et al., 1999; Montabana and Agard, 2014). Particularly, the PhuZ$_{201}$ N terminus faces the exterior of the filament, and most of the C terminus (H11 and the C-terminal tail) faces the interior (Figures 3A and 3B). The N-terminal domain defines the outer surface of the filament, whereas the lumen is dominated by the activation domain, H11, and the C-terminal tail. The acidic knuckle is largely sequestered from solvent along the axis of the filament (except for E310) but, of course, would be fully solvent exposed at the plus end of the filament. The crescent-shaped subunits are

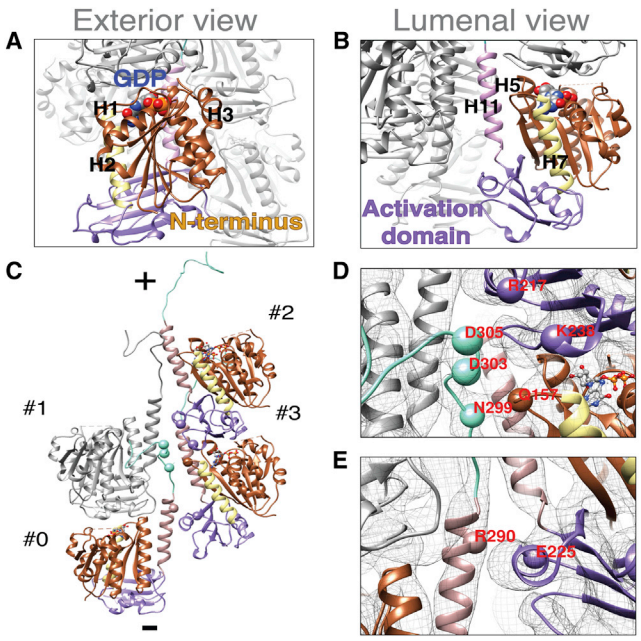

Figure 3. PhuZ$_{201}$ Subunit Is Uniquely Oriented within the Filament and Makes Lateral Contacts through a Set of Conserved Residues

PhuZ$_{201}$ subunit is colored by the following scheme: brown, N-terminal domain; yellow, H7; violet, activation domain; rosy brown, H11; cyan, C-terminal tail; GDP:Mg^{2+} is colored by element. Cryo-EM map density is represented as a gray mesh (D and E).

(A and B) Exterior (A) and lumenal (B) views of a subunit within the filament.

(C–E) Lateral contacts within the three-stranded filament. Alpha carbons of the residues predicted to mediate lateral contacts are shown as spheres.

(C) C terminus of subunit #0 makes contacts with longitudinal subunit #1 and with subunits #2 and #3 of a lateral dimer. Filament ends are designated as (+) end with the C termini and (−) end with the activation domains.

(D) D303 and D305 of subunit #0 contact K238 and R217 of subunit #2, respectively; N299 of subunit #0 contacts Q157 of subunit #3.

(E) R290 of subunit #0 contacts E225 of subunit #3.

See also Figure S2.

oriented such that the curved helices H1, H2, and H3 construct the outer surface of the filament (Figure 3A), and the straight long helices H5, H7, and H11 (Figure 3B), surrounding the large acidic pocket left in place of the missing H6, outline the lumen. The filament is not a hollow tube, as its lumen is filled by the map densities connecting the protofilaments and the densities corresponding to the C termini (Figure 2B; Movie S1). The unique monomer orientation arises as a consequence of distinctive lateral interactions for a tubulin/FtsZ-like filament.

On the basis of the fit model, the C terminus of each PhuZ$_{201}$ subunit contacts three other subunits: a laterally adjacent dimer as well as the adjacent longitudinal subunit (Figure 3C). To aid in describing the unique interactions a subunit makes within the three-stranded filament, we label subunits contacted by a subunit (#0) as follows: #1 is a longitudinally adjacent subunit within the same protofilament, #2 is a laterally adjacent subunit at the plus end, and #3 is a laterally adjacent subunit at the minus end of the neighboring protofilament (Figure 3C). As described previously, the nine, primarily charged, most distal C-terminal residues of the acidic knuckle of subunit #0 contact subunit #1 (Kraemer et al., 2012), while at least three other contacts are formed between other residues in the C-terminal tail and residues in subunits #2 and #3. These interactions are electrostatic/polar in nature and contribute 680 Å^2/subunit of buried surface area. In detail, D303 and D305 of the acidic knuckle of subunit #0 were found to be in close proximity to K238 of H10 and R217 of H9 of subunit #2 (Figure 3D). Additionally, N299 of subunit #0 seems to form a polar interface with Q157, found in the S6-H7 loop of subunit #3, while R290 of H11 (subunit #0) contacts E225 in the H9-S8 loop of subunit #3 (Figures 3D and 3E). The aforementioned fitting adjustments to the C terminus were essential to make these interstrand contacts, thereby providing insights into structural rearrangements that accompany filament formation.

Mutations to Conserved Residues in the Predicted Lateral Interface Disrupt PhuZ$_{201}$ Filament Formation

To test the validity of the predicted lateral interaction surfaces, point mutations to some of the residues were generated, and mutants were tested for the ability to polymerize by right-angle light scattering, high-speed pelleting assay, and negative-stain EM. On the basis of proximity in the model, alanine mutations were made to putative salt-bridge-forming residues D303 and D305 within the conserved IIDXDD motif and the also well-conserved R217 (Figure S2). Importantly, D303 and D305 were solvent exposed in the PhuZ$_{201}$ crystal structure and consequently did not appear to be relevant for the formation of longitudinal interactions (Kraemer et al., 2012). The D303A mutation had a mild effect on PhuZ$_{201}$ assembly, with a critical concentration of 3.7 ± 0.2 μM and a slightly longer lag phase than that observed for the wild-type (Table S1; Figure 4A). The D305A mutation was more severe, with the mutant assembling at a critical concentration of 4.1 ± 0.4 μM (Table S1). The D305A assembly curve had a long lag phase and decayed soon after it reached its peak, which suggested assembly of less stable filaments (Figure 4A). Combining these mutations had an additive effect, with the D303A/D305A double mutant polymerizing with a critical concentration of 9.4 ± 0.3 μM (Table S1), a lag phase longer than either of the single mutants, and a rising and falling polymerization curve similar to the one measured for D305A, likely indicative of polymer instability (Figure 4A). To examine unstable structures the double mutant formed, it was assembled in excess GMPCPP and imaged using negative-stain EM. The mutant still formed three-stranded filaments, although very rarely (Figure S3A). In contrast, the R217A mutation resulted in no detectable polymerization measured by right-angle light scattering, even at concentrations as high as 30 μM (Figure 4A). In the presence of GMPCPP, PhuZ$_{201}$-R217A formed only amorphous structures (Figure S3B).

These observations supported the relevance of R217 and D305, which are predicted by the model to form a salt bridge stabilizing the lateral interface (Figure 3D). To test this prediction, individual charge reversal mutations, R217D and D305R, along with the charge-swap double mutant R217D/D305R, were generated and their functional consequences examined. Similar to the R217A mutant, PhuZ$_{201}$-R217D was unable to form any detectable polymer at concentrations up to 30 μM (Figures 4A and 4B) but formed amorphous structures in GMPCPP (Figure 4C). The D305R mutant was also severely polymerization compromised (Figures 4A and 4B), with a critical concentration

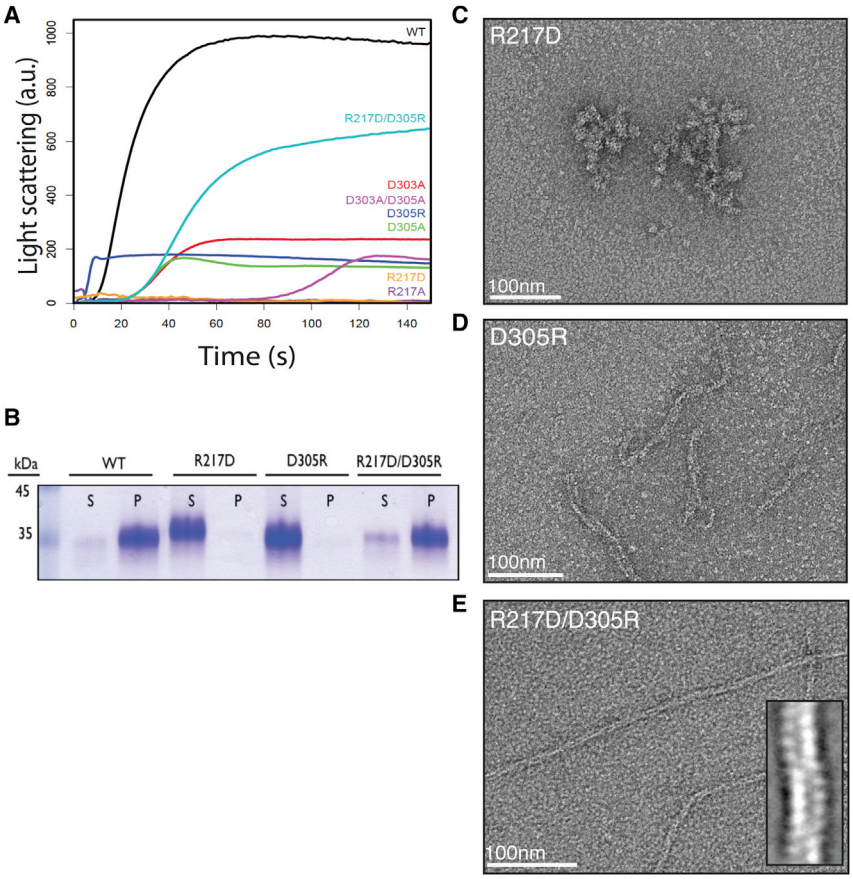

Figure 4. Mutations to Residues Predicted to Mediate Lateral Contacts Disrupt PhuZ$_{201}$ Assembly In Vitro

(A) Right-angle light-scattering traces of PhuZ$_{201}$ wild-type (WT) and mutants polymerized in 1 mM GTP. The following concentrations were used: 3 μM WT in black, 5 μM D303A in red, 7 μM D305A in green, 9 μM D305R in dark blue, 30 μM R217A in purple, 30 μM R217D in orange, 10 μM D303A/D305A in violet, and 6 μM R217D/D305R in cyan.

(B) Polymerization of PhuZ$_{201}$ mutants in excess GTP was assayed by high-speed pelleting assay as described in the Experimental Procedures, with supernatant (S) and pellet (P) fractions analyzed by SDS-PAGE. (A) and (B) Charge reversal mutant R217D/D305R partially restores the ability to form filaments.

(C–E) Sections of micrographs of negatively stained PhuZ$_{201}$ mutants polymerized in excess GMPCPP. PhuZ$_{201}$ single mutants R217D (C) and D305R (D) are unable to form three-stranded filaments, but the double mutant R217D/D305R (E) assembles three-stranded filaments (inset).

See also Table S1 and Figure S3.

of 8.0 ± 0.2 μM (Table S1). The mutant no longer appeared to assemble into three-stranded filaments, but formed rare, short and twisted structures with a variable number of strands (Figure 4D). PhuZ$_{201}$-D305R polymerized with almost no lag phase and was unstable in GTP, suggesting that the structures it formed lacked key stabilizing interactions (Figure 4A). In contrast, combining the R217D and D305R mutations recovered polymerization (Figures 4A and 4B), albeit with a significantly higher critical concentration (5.9 ± 0.3 μM) (Table S1). Importantly, the double mutant also restored formation of three-stranded filaments (Figure 4E). These observations support the existence of a salt bridge between R217 and D305 and confirm its importance for polymer assembly.

To test whether PhuZ$_{201}$ uses the same surfaces for its assembly in vivo, we examined the ability of these mutant proteins to make filaments in *P. chlororaphis* cells. Fusion constructs of the wild-type and the mutant versions of PhuZ$_{201}$ fused to green fluorescent protein were generated and conditionally expressed from a plasmid. Both the D303A and D305A mutations impaired filament formation in vivo (Figures 5A and 5B), with the D305A single mutant and the D303A/D305A double mutant having the most severe effects. Additionally, the R217A, R217D, or D305R mutant completely eliminated filament formation in cells (Figures 5C and 5D). In accordance with the in vitro observations, the double mutant R217D/D305R resulted in a partial restoration of the ability to assemble filaments in about 1% of cells when expressed at high levels (grown in the presence of 2% arabinose) (Figures 5C and 5D). Those filaments that formed were dynamic and appeared to be similar to the wild-type filaments. The in vivo observations are completely consistent with the in vitro assembly behavior of the mutants, suggesting that PhuZ$_{201}$ assembles into filaments with at least three strands. These findings demonstrate the importance of the conserved residues for the establishment and stability of lateral interactions and suggest a conserved mechanism for the filament formation within the PhuZ family of tubulin homologs.

Comparison of the Filament Structure with Crystal Structures Reveals Origins of Twist and Movement of the C-terminal Tail

As demonstrated nicely by a morph (Movie S2) between the crystallographic protofilaments (3R4V and 3ZBQ) (Kraemer et al., 2012; Aylett et al., 2013) and the structure of the three-stranded filament, the PhuZ$_{201}$ dimer undergoes a striking rearrangement upon incorporation into the filament lattice. PhuZ$_{201}$ subunits form a canonical tense tubulin/FtsZ longitudinal interface in the presence of the γ-phosphate (Movie S2). Within the PhuZ$_{201}$-GMPCPP filament, a subunit buries 840 Å^2 surface area at the tense interface, as opposed to 188 Å^2/subunit at the relaxed interface observed within the PhuZ$_{201}$-GDP crystal (Kraemer et al., 2012) (Figure 6A). To compare subunit packing within the filament with the post-GTP-hydrolysis arrangement depicted within the PhuZ$_{KZ}$-GDP (3ZBQ) protofilament (having no twist and 43.5 Å pitch) (Aylett et al., 2013), we modeled the straight protofilament by separately superimposing two PhuZ$_{201}$ monomers over a PhuZ$_{KZ}$ longitudinal dimer using the N-terminal domains (residues 2-160 in PhuZ$_{201}$ and 4-173 in PhuZ$_{KZ}$), but excluding the activation domains and the C termini, for alignment. The posthydrolysis longitudinal interface in the

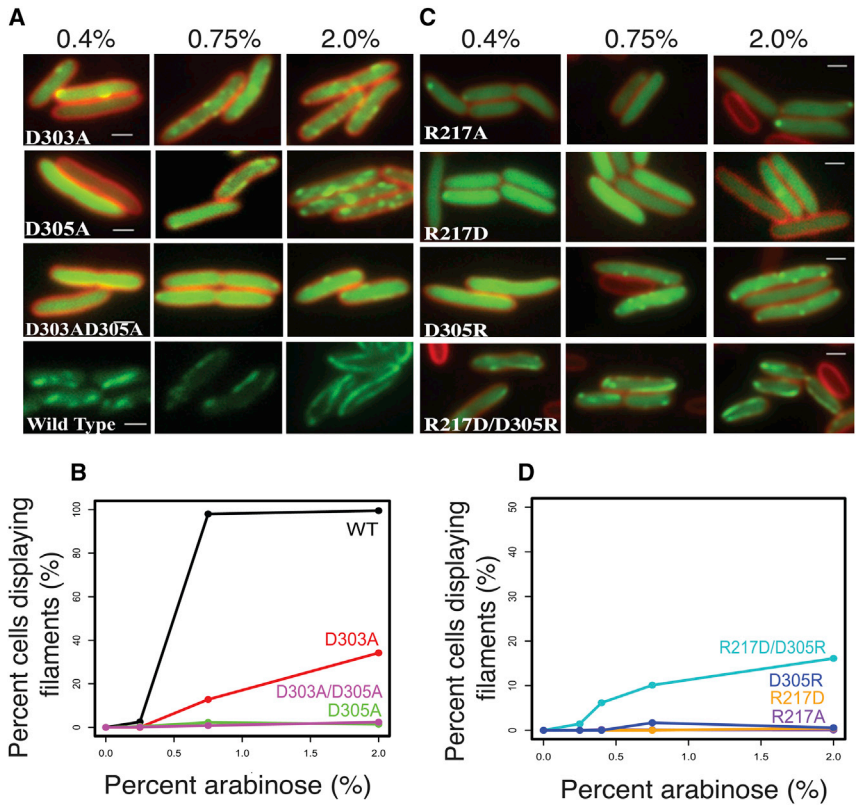

Figure 5. PhuZ$_{201}$ Assembles via the Same Set of Lateral Surfaces In Vivo as In Vitro

(A and C) Fluorescent micrographs of uninfected *P. chlororaphis* cells expressing various GFP-PhuZ$_{201}$ mutant constructs. (A) Shown are the three tail mutants D303A, D305A, and the double mutant D303A/D305A at 0.4%, 0.75%, and 2% arabinose induction. WT PhuZ$_{201}$ is in the last strip for comparison. All mutants have compromised filament formation.

(B) Quantitation of data in (A) indicating that of the three mutants, only D303A shows any appreciable polymerization at 2% arabinose. (C) Shown are the four tail mutants R217A, R217D, D305R, and the double mutant R217D/D305R at 0.4%, 0.75%, and 2% arabinose induction. The single mutants are unable to make filaments, but the charge reversal in the double mutant partially restores filament formation.

(D) Quantitation of the concentration data from (C). Scale bars represent 1 μm.

PhuZ$_{KZ}$-like dimer model buries 930 Å^2/subunit. While the ~11° twist between longitudinally adjacent subunits and the slightly smaller pitch of the PhuZ$_{201}$-GMPCPP filament (43.2 Å) results in a small decrease in the longitudinal buried surface area compared to the PhuZ$_{KZ}$-like subunit packing, the overall effect is to tighten contacts around the GTP-binding pocket. Within a GMPCPP dimer, the contact surface between H10 and H7 is weakened, but tighter contacts are established between the T7 and the S2-S3 loops and the catalytic N terminus of H8 with the T3 loop of subunits #1 and #0, respectively (Figure 6B). Measured distances from the catalytic Asp on the T7 loop to the β-phosphate are the same in the PhuZ$_{201}$-GMPCPP dimer and the PhuZ$_{KZ}$-like state: 6.7 and 6.8 Å, respectively, but much shorter than in PhuZ$_{201}$-GDP (10.5 Å) (Figure 6B).

The other significant consequence of filament formation is that both the twist and the structural rearrangement of the C terminus contribute to the establishment of the lateral interface (Movie S2). The twist between longitudinal subunits brings the finger-like IIDXDD motif of subunit #0 and the shape-complementary basic cavity, defined by R217 and K238, of laterally adjacent subunit #2, ~5 Å closer toward each other. Moreover, the C terminus of subunit #0 pulls away from the side of longitudinal subunit #1 to form lateral interactions with subunits #2 and #3 (Figure 6A and Movie S2). Although the majority of the contacts made by residues of the acidic knuckle remain intact, the remaining residues of the C-terminal tail and H11 (K294-D306) separate to establish lateral interactions (Figure 6A). This movement shifts the C$^{\alpha}$ of N299 of subunit #0 ~2 Å closer toward the C$^{\alpha}$ of Q157 of subunit #3, placing the two alpha carbons ~5 Å apart. The C-terminal helix, H11, of subunit #0 is also tilted toward the central axis of the filament to form a putative salt bridge between R290 and E225 of subunit #3. The net result of these C-terminal tail movements is a significant loss of the intrasubunit buried surface area: 780 Å^2/subunit in the filament versus 1,226 Å^2/subunit in the crystal (Kraemer et al., 2012) (Figure 6A). This energetically unfavorable loss of intraprotofilament interactions is compensated for by the establishment of new lateral interactions, resulting in an overall larger surface area buried per subunit in the three-stranded filament versus the crystallographic protofilament.

DISCUSSION

Although the core tertiary structure is well conserved in the tubulin/FtsZ superfamily, a high degree of sequence variation, including insertions and deletions in loops and termini, leads to divergent filament morphologies. Because only the structures of microtubules and TubZ have been determined to even moderate resolution (Sui and Downing, 2010; Montabana and Agard, 2014), we are just beginning to understand how these sequence variations define polymer architecture. Here, we describe the unique three-stranded filament structure of a phage-encoded tubulin homolog, PhuZ$_{201}$, at 7.1 Å resolution by cryo-EM. Docking the crystal structure of PhuZ$_{201}$-GDP (Kraemer et al., 2012) into the map reveals the critical role the C-terminal tail plays in filament assembly. As previously noted, the acidic residues in the tail of one subunit (#0) bind to a well-defined basic pocket in the longitudinal subunit (#1) to stabilize protofilament interactions (Kraemer et al., 2012). Remarkably, the other solvent-exposed acidic residues, within the conserved IIDXDD motif, are shown here to mediate lateral interactions with both subunits #2 and #3 in adjacent protofilaments. To mediate lateral contacts, the C-terminal tail undergoes a significant conformational rearrangement upon assembly, trading off intraprotofilament interactions for interprotofilament interactions, with only the acidic

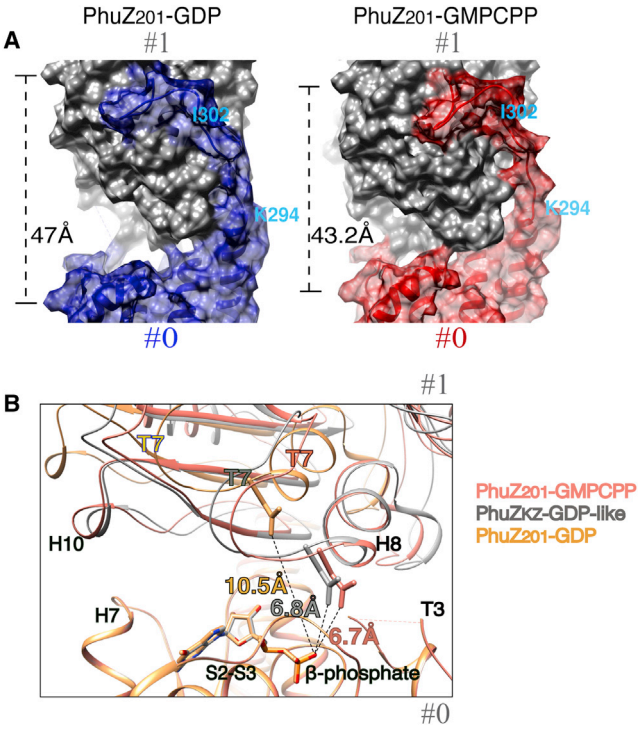

Figure 6. Comparison of the Longitudinal Packing between PhuZ$_{201}$-GDP, PhuZ$_{KZ}$-like-GDP, and the Three-Stranded Filament

Longitudinal subunits within a dimer are labeled #0 and #1.

(A) PhuZ$_{201}$ dimers representative of the packing within the crystal (3R4V) (Kraemer et al., 2012) (left) versus the three-stranded filament (right) are shown as molecular surfaces. (Left) PhuZ$_{201}$ subunit packing within the crystal: the C-terminal tail of subunit #0 in blue forms extensive interactions with the side of subunit #1 in gray. The dimer has a relaxed longitudinal interface with 47 Å spacing. (Right) PhuZ$_{201}$ subunit packing within the three-stranded filament: the C-terminal tail of subunit #0 in red forms weak longitudinal contacts with the side of subunit #1 in gray. The dimer has a tense canonical tubulin/FtsZ longitudinal interface with 43.2 Å spacing.

(B) Magnified view of the longitudinal interfaces in PhuZ$_{201}$-GMPCPP dimer in salmon, PhuZ$_{201}$ mimicking subunit packing as in a PhuZ$_{KZ}$-GDP dimer (3ZBQ) (Aylett et al., 2013) in gray, and a PhuZ$_{201}$-GDP dimer (3R4V) (Kraemer et al., 2012) in yellow. The dimers were superimposed via the residues (2–271) corresponding to the N-terminal domains and the activation domains, but excluding the residues corresponding to the C termini, of the subunits at minus ends. Measured distances from the catalytic Asp on the T7 loop to the β-phosphate are 6.7 Å in the three-stranded filament, 6.8 Å in PhuZ$_{KZ}$-GDP-like state, and 10.5 Å in PhuZ$_{201}$-GDP.

See also Movie S2.

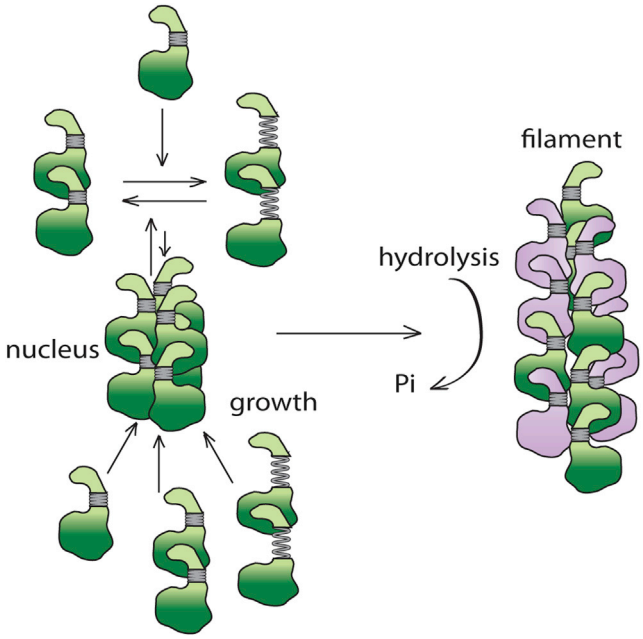

Figure 7. Model for PhuZ Assembly

GTP-bound PhuZ is in green, and GDP-bound is in purple. PhuZ monomers as seen in the crystal (3ZBP) (Aylett et al., 2013) assemble dimers with a tense longitudinal interface as in the crystal structure (3ZBQ) (Aylett et al., 2013) or the relaxed interface as in the crystal structure (3R4V) (Kraemer et al., 2012). Three dimers form a hexameric nucleus with subunits displaying the intramolecular contacts as seen in the pseudo-atomic model described in this work. The nucleus grows by the addition of dimers and monomers. GTP is hydrolyzed soon after filament assembly.

knuckle retaining its original longitudinal contacts. While tubulin C termini have been described to be involved in binding interactions with nontubulin partners, this use of a C terminus in defining filament architecture, leading to cooperative assembly, represents a new polymerization mechanism.

Importantly, residues forming both the lateral and longitudinal contacts observed here for PhuZ$_{201}$ are conserved in the related phage tubulins PhuZ$_{PA3}$ and PhuZ$_{KZ}$ (Figure S2, S4A, and S4B). While D303, D305, and R217 are found in all three homologs, lysine (K238) is conservatively substituted for arginine in PhuZ$_{PA3}$ and PhuZ$_{KZ}$. Moreover, the putative polar interface most likely exists in PhuZ$_{PA3}$ and PhuZ$_{KZ}$ as well, because N299 and Q157 are identical or have conservative substitutions in these proteins. Finally, the putative electrostatic interface between R290 and E225 is conserved in PhuZ$_{KZ}$, and although R290 is missing in PhuZ$_{PA3}$, there is an arginine one helical turn away (R294) that could interact with E225. Thus, on the basis of conservations of critical interactions, we propose that both PhuZ$_{KZ}$ and PhuZ$_{PA3}$ form similar three-stranded polymers. In support of this, a 2D class average of segments from PhuZ$_{PA3}$ filaments shows a pattern characteristic of a three-stranded polymer (Figure S4C; Figure 1A). In contrast, the fourth, more evolutionary divergent PhuZ family homolog, PhuZ$_{EL}$, encoded by bacteriophage ϕEL that does not belong to the "ϕKZ-like viruses" genus (Lavigne et al., 2009), shows significant variations at the lateral interface, suggestive of a different filament architecture. We had also previously identified a subset of proteins (Cb, Ck, Ca, and Cl) belonging to a family of *Clostridial* chromosomal tubulin homologs that also have acidic knuckle sequences (Kraemer et al., 2012). Intriguingly, these tubulins show conservation in a number of the key interactions that define the polymer contacts identified here (Figure S2), suggesting that their filament morphologies may be related.

The structural and kinetic data from this study and the three structures described in previous studies (Kraemer et al., 2012; Aylett et al., 2013) provide insight into the mechanism of PhuZ filament assembly and the role of the γ-phosphate in setting up the metastability required for filament dynamics (Figure 7). We propose that these structures relate to distinct stages in

the assembly process. First, GTP-bound monomers ($PhuZ_{KZ}$ 3ZBP) (Aylett et al., 2013) would associate via the extensive interactions between the C-terminal tail of one monomer (#0) and binding pocket of the #1 monomer forming longitudinal dimers ($PhuZ_{201}$ 3R4V) with a relaxed subunit-subunit interface (Kraemer et al., 2012). In the presence of GTP, this state is likely in equilibrium, with a compacted form corresponding to a straight tense interface observed within the crystallographic protofilament ($PhuZ_{KZ}$ 3ZBQ) (Aylett et al., 2013). The linker allows the longitudinal subunit-subunit interface to elastically transition between these two states: relaxed (47Å) (Kraemer et al., 2012) and tense (~43.5 Å) (Aylett et al., 2013). Three of these dimers then laterally associate, further reorganizing the C termini, twisting and moving out their C termini to fulfill all of the filament contacts within the hexameric nucleus. The energetically unfavorable loss of longitudinal contacts and strain from the twisting are stabilized by the newly formed lateral interactions and the presence of the γ-phosphate. The filament then grows by further addition of GTP-bound monomers and dimers. We propose that upon GTP hydrolysis, strain resulting from twisting and displacement of C-terminal interactions within each subunit is trapped by cooperative lattice interactions, leading to metastability and highly dynamic filaments.

Previous work had shown that dynamic PhuZ filaments are necessary for clustering and centering phage particles within the host bacterial cell. Interfering with filament dynamics leads to offset fragmented clusters and a significant decrease in phage burst size (Kraemer et al., 2012). Given its conservation among the members of the PhuZ family, the specific choice of a three-stranded architecture must somehow be particularly important for the viral replication cycle. One possibility is that the three-stranded filament morphology could provide a stiffer structure than the more common two-stranded architecture of plasmid-segregating prokaryotic actins to move such very large phage particles (≥200 nm) or their genomes in a crowded cytoplasm. Another intriguing possibility is that the filament's three-stranded architecture might be a structural adaptation that facilitates interactions directly, or indirectly through an adaptor protein, with three-fold symmetry centers within the capsid or tail.

There are a number of potential protein-protein interaction surfaces in PhuZ that could be functionally important. Of particular note is the acidic C-terminal tail. Within the body of the filament, the tail is sequestered in the lateral interface, but it is completely exposed at the plus end of the filament. Thus, this could provide a unique polar binding site for linkage to DNA or the phage in a manner reminiscent of the interaction between ParM filaments and the end-binding ParRC complexes that connect the filament to plasmid DNA (Garner et al., 2007; Gayathri et al., 2013). Alternatively, among the conserved surfaces exposed along the filament is an acidic patch, defined by D235, D259, and D263, that is in close proximity to the lateral interface formed by the IIDXDD motif and the basic pocket defined by R217 and K238 (Figure S4B).

The unusual three-stranded architecture of the filament and the novel role of the C terminus pose intriguing questions about PhuZ filament dynamics and its biological role. Although the filament structure suggests how the energy of GTP is stored within the helical lattice—through the bending of the C terminus and the supertwist—how this structure defines the dynamic properties of the polymer remains to be explained. Future high-resolution structural studies of $PhuZ_{201}$ bound to different nucleotides, both in monomeric and filamentous forms, complemented by kinetic solution and modeling studies are needed to answer this question. Beyond this, the major issues going forward concern the physical and possible regulatory coupling of polymer dynamics to phage maturation and host cell positioning. Whether this involves only phage-encoded proteins or whether host proteins are also recruited remains to be determined.

EXPERIMENTAL PROCEDURES

Protein Expression and Purification

The genes encoding $PhuZ_{PA3}$ and $PhuZ_{201}$ were cloned into pET28a (+) with a 6-His tag on the N terminus and expressed in BL21(DE3) cells under an isopropyl β-D-1-thiogalactopyranoside (IPTG)-inducible T7 promoter. The $PhuZ_{201}$ mutants were generated by two primer-site-directed mutagenesis PCR. IPTG (1 mM) was added once cells reached an optical density at 600 nm of 0.7 at 37°C, and protein was allowed to express for 8 hr at 16°C before the cells were pelleted. Cells were lysed in a buffer containing 250 mM KCl, 50 mM HEPES (pH 7.4), 1 mM $MgCl_2$, 10% glycerol, and 1 mM dithiothreitol (DTT). EDTA-free protease inhibitor tablets were included during lysis. Imidazole (250 mM) was added to elute the protein from the nickel nitrilotriacetic acid resin. The 6-His tag was cleaved overnight at 4°C by thrombin protease, followed by gel filtration chromatography (Superdex 200) in a buffer as described previously, but omitting glycerol.

Negative-Stain EM

PhuZ (10 μM) was polymerized in BRB80 (pH 7.2) with the addition of 1 mM GMPCPP for 2 min at room temperature. Four microliters of polymerized protein was applied to carbon-coated grids after glow discharging, unbound sample was washed away with water, and grids were stained with 0.75% uranyl formate. Micrographs were collected on Tecnai T12 or T20 microscopes (FEI Company) using an accelerating voltage of 120 or 200 kV and magnification of 52,000× or 50,000×, respectively. Images were recorded with a 4k × 4k charge-coupled device (Gatan).

Sample Preparation and Data Collection for Cryo-EM

Twenty micromolar protein was polymerized in 50 mM HEPES (pH 8), 125 mM KCl, 5 mM $MgCl_2$, 5% glycerol, and 1 mM GMPCPP for 1 min at room temperature. Two microliter samples were applied on C-flat holey carbon grids and plunge-frozen into liquid ethane using Vitrobot (FEI Company). Micrographs were collected on Tecnai F20 operating at 200 V. Images were recorded with an 8k × 8k TemCam-F816 camera (TVIPS) at a magnification of 62,000×, corresponding to a pixel size of 1.204 Å. Total electron dose was in the range of 25 to 30 e^- per $Å^2$, and images were acquired over an underfocus range of 0.7 to 2.5 μm.

Image Processing

CTFFIND was used to determine defocus parameters (Mindell and Grigorieff, 2003). Contrast transfer function (CTF) was corrected by applying a Weiner filter to the entire micrograph. Four hundred sixty-one cryo-EM micrographs were CTF-corrected, and 460-pixel segments with 40-pixel shift for each segment were extracted from the micrographs. The large segment size was chosen to maximize the accuracy of image alignment in the initial rounds of reconstruction. Reconstructions were determined by iterative helical real space reconstruction (Egelman, 2000), performed essentially as described by Egelman (2000), but following the "gold standard" procedure (Scheres and Chen, 2012) with two models refined independently to optimize resolution estimates and minimize data overfitting. SPIDER (Frank et al., 1996) was used for multireference alignment, projection matching, and back projection, and the hsearch_lorentz program was used for symmetry search (Egelman, 2000). A preliminary reconstruction (reconstructed without the application of the "gold standard" procedure) of the filament starting from a plain cylinder was carried out. Then, the obtained model was low-pass-filtered to 40 Å and used as starting references for the reconstruction (with

Table 1. Strains and Plasmids Used

Strain	Organism	Plasmid/Mutation	Citation
ME41	*P. chlororaphis* 200B-1	pME28/GFP-PhuZ	Kraemer et al., 2012
ME91	*P. chlororaphis* 200B-1	pME57/GFP-PhuZD303A	this paper
ME92	*P. chlororaphis* 200B-1	pME58/GFP-PhuZD305A	this paper
ME93	*P. chlororaphis* 200B-1	pME61/GFP-PhuZD303305A	this paper
ME102	*P. chlororaphis* 200B-1	pME62/GFP-PhuZR217A	this paper
ME103	*P. chlororaphis* 200B-1	pME63/GFP-PhuZR217D	this paper
ME104	*P. chlororaphis* 200B-1	pME64/GFP-PhuZD305R	this paper
ME105	*P. chlororaphis* 200B-1	pME65/GFP-PhuZR217DD305R	this paper

the application of the "gold standard" procedure) of the cryo-EM map shown in this work. Reference projections were generated at 2° intervals perpendicular to the helix axis and up to 12° out-of-plane tilt. The segments were rejected on the basis of the excessive shifts perpendicular to the helix axis and rotations deviating from average rotations for filaments. Filaments containing less than 70% (initial rounds of alignments) or 90% (final rounds of alignment) segments determined as having the same polarity were discarded. After ten initial rounds of alignment, the segments were recentered, applying the determined in the tenth round of refinement shift values, with respect to the helix axis. Then, the segments were masked to 260 pixels along the helix axis, to minimize the effect of filament bending, and 120 pixels perpendicular to the axis with a cosine-edged mask. The initial rounds of projection matching were carried out using data binned by a factor of two, while the final rounds were performed on unbinned images. A Fourier shell correlation curve was calculated between the two reconstructions at the end of each refinement round, and the volumes were low-pass-filtered to an estimated resolution, and then these volumes were used as the references for the next round of refinement. At the last round of refinement, the half reconstructions were combined to obtain the final cryo-EM model. A total of 69,729 unique $PhuZ_{201}$ subunits contributed to the final reconstruction. The map was low-pass-filtered to 7.1 Å and sharpened with a −1,200 $Å^2$ B-factor. Although this is a somewhat large value, even at this level of sharpening, the map had very little noise. Molecular graphics and analyses were performed with UCSF Chimera (Pettersen et al., 2004). Noise in the final 3D map was eliminated for display purposes using the "Hide Dust" option in UCSF Chimera (Pettersen et al., 2004).

Light Scattering

Protein was thawed and spun at 80,000 rpm in a TLA-100 rotor (Beckman) at 4°C before all light scattering assays. Right-angle light scattering was conducted by mixing $PhuZ_{201}$ with BRB80 (pH 7.2) (80 mM PIPES, 1 mM $MgCl_2$, 1 mM EGTA [pH 7.2] with KOH) containing GTP using a microvolume stopped-flow system designed in house. An illumination wavelength of 532 nm was used. Critical concentrations were determined by plotting the maximum intensity versus $PhuZ_{201}$ concentration for each mutant. The x intercept of this plot was used as the critical concentration.

Pelleting Assay

Protein samples were spun down for 5 min at 4°C at 80,000 rpm in a TLA-100 rotor (Beckman) to remove protein aggregates. Protein (10 μM) was polymerized in BRB80 (pH 7.2), 1 mM DTT, and 2 mM GTP for 2 min at room temperature and spun down at 80,000 rpm for 30 min at 4°C. Supernatant and pellet were analyzed by SDS-PAGE electrophoresis using 12% gel, stained with a Coomassie reagent.

Strain Construction

All mutant strains used (Table 1) were constructed using site-directed mutagenesis PCR on the previously published pME28 (Kraemer et al., 2012), which is the wild-type GFP-$PhuZ_{201}$ genetic fusion borne in the broad range *Pseudomonad* vector pHERD30T (Qiu et al., 2008). *P. chlororaphis* 200B-1 cells were prepared and transformed as in Howard et al. (2007).

Filament Expression Levels in Mutant Strains

P. chlororaphis cells bearing the respective mutant plasmids (Table 1) were grown overnight at 30°C on a hard agar plate (Thomas et al., 2008) supplemented with gentamicin sulfate at 25 μg/ml. To prepare the microscope slides, agarose pads were made with 25% Luria broth, 75% distilled H_2O, 13 mg/ml agarose, 0.1 μl/ml FM4-64 membrane dye, 0.1 μl/ml gentamicin (concentration 25 μg/ml), and the appropriate amount of arabinose. A single colony of cells was then transferred to the slide pad and incubated for 2 hr at 30°C in a humidified chamber. Images of the live cells after 2 hr of incubation were analyzed using ImageJ for the total number of cells and the number of cells expressing filaments at different arabinose concentrations. Cells were imaged on a DeltaVision Deconvolution system (Applied Precision/GE) IX70 Olympus microscope with 100× 1.4 Plan Apo lens.

ACCESSION NUMBERS

The EM reconstruction and atomic coordinates have been deposited in the Electron Microscopy Data Bank and the RCSB Protein Data Bank with accession codes EMD-5783 and 3J5V, respectively.

SUPPLEMENTAL INFORMATION

Supplemental Information includes Supplemental Experimental Procedures, four figures, one table, and two movies and can be found with this article online at http://dx.doi.org/10.1016/j.str.2014.02.006.

ACKNOWLEDGMENTS

We thank Justin Kollman and Sam Li for invaluable discussions on image processing, Justin Kollman and Xueming Li for help with image collection, Michael Braunfeld and Bettina Keszthelyi for help with tomographic data collection and processing, and Pascal Wassam for maintenance of systems hardware and software. J.A.K. was supported by the Genentech Foundation Predoctoral Fellowship and the Achievement Rewards for College Scientists Foundation Award. This work was supported by the Howard Hughes Medical Institute (to D.A.A.) and National Institutes of Health grants GM031627 (to D.A.A.), R01GM073898 (to J.P.), and GM104556 (to J.P. and D.A.A.).

Received: December 5, 2013
Revised: January 31, 2014
Accepted: February 11, 2014
Published: March 13, 2014

REFERENCES

Aylett, C.H., Wang, Q., Michie, K.A., Amos, L.A., and Löwe, J. (2010). Filament structure of bacterial tubulin homologue TubZ. Proc. Natl. Acad. Sci. USA *107*, 19766–19771.

Aylett, C.H., Lowe, J., and Amos, L.A. (2011). New insights into the mechanisms of cytomotive actin and tubulin filaments. Int. Rev. Cell Mol. Biol. *292*, 1–71.

Aylett, C.H., Izoré, T., Amos, L.A., and Löwe, J. (2013). Structure of the tubulin/FtsZ-like protein TubZ from Pseudomonas bacteriophage ΦKZ. J. Mol. Biol. *425*, 2164–2173.

Bramhill, D., and Thompson, C.M. (1994). GTP-dependent polymerization of Escherichia coli FtsZ protein to form tubules. Proc. Natl. Acad. Sci. USA *91*, 5813–5817.

Egelman, E.H. (2000). A robust algorithm for the reconstruction of helical filaments using single-particle methods. Ultramicroscopy *85*, 225–234.

Egelman, E.H. (2007). The iterative helical real space reconstruction method: surmounting the problems posed by real polymers. J. Struct. Biol. *157*, 83–94.

Flyvbjerg, H., Jobs, E., and Leibler, S. (1996). Kinetics of self-assembling microtubules: an "inverse problem" in biochemistry. Proc. Natl. Acad. Sci. USA *93*, 5975–5979.

Fokine, A., Battisti, A.J., Bowman, V.D., Efimov, A.V., Kurochkina, L.P., Chipman, P.R., Mesyanzhinov, V.V., and Rossmann, M.G. (2007). Cryo-EM study of the Pseudomonas bacteriophage phiKZ. Structure *15*, 1099–1104.

Frank, J., Radermacher, M., Penczek, P., Zhu, J., Li, Y., Ladjadj, M., and Leith, A. (1996). SPIDER and WEB: processing and visualization of images in 3D electron microscopy and related fields. J. Struct. Biol. *116*, 190–199.

Garner, E.C., Campbell, C.S., Weibel, D.B., and Mullins, R.D. (2007). Reconstitution of DNA segregation driven by assembly of a prokaryotic actin homolog. Science *315*, 1270–1274.

Gayathri, P., Fujii, T., Namba, K., and Löwe, J. (2013). Structure of the ParM filament at 8.5Å resolution. J. Struct. Biol. *184*, 33–42.

Howard, G.T., Mackie, R.I., Cann, I.K., Ohene-Adjei, S., Aboudehen, K.S., Duos, B.G., and Childers, G.W. (2007). Effect of insertional mutations in the pueA and pueB genes encoding two polyurethanases in Pseudomonas chlororaphis contained within a gene cluster. J. Appl. Microbiol. *103*, 2074–2083.

Kraemer, J.A., Erb, M.L., Waddling, C.A., Montabana, E.A., Zehr, E.A., Wang, H., Nguyen, K., Pham, D.S., Agard, D.A., and Pogliano, J. (2012). A phage tubulin assembles dynamic filaments by an atypical mechanism to center viral DNA within the host cell. Cell *149*, 1488–1499.

Krylov, V.N., Dela Cruz, D.M., Hertveldt, K., and Ackermann, H.W. (2007). "phiKZ-like viruses", a proposed new genus of myovirus bacteriophages. Arch. Virol. *152*, 1955–1959.

Lavigne, R., Darius, P., Summer, E.J., Seto, D., Mahadevan, P., Nilsson, A.S., Ackermann, H.W., and Kropinski, A.M. (2009). Classification of Myoviridae bacteriophages using protein sequence similarity. BMC Microbiol. *9*, 224.

Li, Z., Trimble, M.J., Brun, Y.V., and Jensen, G.J. (2007). The structure of FtsZ filaments in vivo suggests a force-generating role in cell division. EMBO J. *26*, 4694–4708.

Löwe, J., and Amos, L.A. (1999). Tubulin-like protofilaments in Ca2+-induced FtsZ sheets. EMBO J. *18*, 2364–2371.

Lu, C., Reedy, M., and Erickson, H.P. (2000). Straight and curved conformations of FtsZ are regulated by GTP hydrolysis. J. Bacteriol. *182*, 164–170.

Mindell, J.A., and Grigorieff, N. (2003). Accurate determination of local defocus and specimen tilt in electron microscopy. J. Struct. Biol. *142*, 334–347.

Montabana, E.A., and Agard, D.A. (2014). Bacterial tubulin TubZ-Bt transitions between a two-stranded intermediate and a four-stranded filament upon GTP hydrolysis. Proc. Natl. Acad. Sci U S A. Published online February 14, 2014. http://dx.doi.org/10.1073/pnas.1318339111.

Ni, L., Xu, W., Kumaraswami, M., and Schumacher, M.A. (2010). Plasmid protein TubR uses a distinct mode of HTH-DNA binding and recruits the prokaryotic tubulin homolog TubZ to effect DNA partition. Proc. Natl. Acad. Sci. USA *107*, 11763–11768.

Nogales, E., Downing, K.H., Amos, L.A., and Löwe, J. (1998a). Tubulin and FtsZ form a distinct family of GTPases. Nat. Struct. Biol. *5*, 451–458.

Nogales, E., Wolf, S.G., and Downing, K.H. (1998b). Structure of the alpha beta tubulin dimer by electron crystallography. Nature *391*, 199–203.

Nogales, E., Whittaker, M., Milligan, R.A., and Downing, K.H. (1999). High-resolution model of the microtubule. Cell *96*, 79–88.

Oliva, M.A., Martin-Galiano, A.J., Sakaguchi, Y., and Andreu, J.M. (2012). Tubulin homolog TubZ in a phage-encoded partition system. Proc. Natl. Acad. Sci. USA *109*, 7711–7716.

Pettersen, E.F., Goddard, T.D., Huang, C.C., Couch, G.S., Greenblatt, D.M., Meng, E.C., and Ferrin, T.E. (2004). UCSF Chimera—a visualization system for exploratory research and analysis. J. Comput. Chem. *25*, 1605–1612.

Qiu, D., Damron, F.H., Mima, T., Schweizer, H.P., and Yu, H.D. (2008). PBAD-based shuttle vectors for functional analysis of toxic and highly regulated genes in Pseudomonas and Burkholderia spp. and other bacteria. Appl. Environ. Microbiol. *74*, 7422–7426.

Scheres, S.H., and Chen, S. (2012). Prevention of overfitting in cryo-EM structure determination. Nat. Methods *9*, 853–854.

Sui, H., and Downing, K.H. (2010). Structural basis of interprotofilament interaction and lateral deformation of microtubules. Structure *18*, 1022–1031.

Thomas, J.A., Rolando, M.R., Carroll, C.A., Shen, P.S., Belnap, D.M., Weintraub, S.T., Serwer, P., and Hardies, S.C. (2008). Characterization of Pseudomonas chlororaphis myovirus 201varphi2-1 via genomic sequencing, mass spectrometry, and electron microscopy. Virology *376*, 330–338.

Weisenberg, R.C. (1972). Microtubule formation in vitro in solutions containing low calcium concentrations. Science *177*, 1104–1105.

 ©2014 Elsevier Ltd All rights reserved